

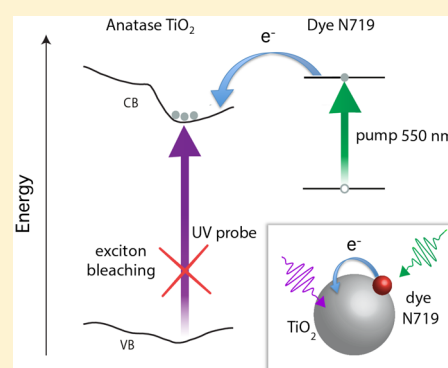
# Interfacial Electron Injection Probed by a Substrate-Specific Excitonic Signature

Edoardo Baldini, Tania Palmieri, Thomas Rossi, Malte Oppermann, Enrico Pomarico, Gerald Auböck, and Majed Chergui\*

Laboratory of Ultrafast Spectroscopy, ISIC and Lausanne Centre for Ultrafast Science (LACUS), École Polytechnique Fédérale de Lausanne, CH-1015 Lausanne, Switzerland

## Supporting Information

**ABSTRACT:** Ultrafast interfacial electron transfer in sensitized solar cells has mostly been probed by visible-to-terahertz radiation, which is sensitive to the free carriers in the conduction band of the semiconductor substrate. Here, we demonstrate the use of deep-ultraviolet continuum pulses to probe the interfacial electron transfer, by detecting a specific excitonic transition in both N719-sensitized anatase TiO<sub>2</sub> and wurtzite ZnO nanoparticles. Our results are compared to those obtained on bare nanoparticles upon above-gap excitation. We show that the signal upon electron injection from the N719 dye into TiO<sub>2</sub> is dominated by long-range Coulomb screening of the final states of the excitonic transitions, whereas in sensitized ZnO it is dominated by phase-space filling. The present approach offers a possible route to detecting interfacial electron transfer in a broad class of systems, including other transition metal oxides or sensitizers.



## INTRODUCTION

In the past decade, interfacial electron transfer (ET) between adsorbates and semiconducting transition metal oxide (TMO) substrates has been subject of huge interest for applications in solar energy conversion<sup>1–4</sup> and photocatalysis.<sup>5–7</sup> In the former case, dye-sensitized solar cells (DSSCs), consisting of a dye molecule adsorbed onto the surface of a mesoporous TiO<sub>2</sub> film, have been the most explored systems. Alternative schemes for charge injection, using metallic (e.g., gold) nanoparticles (NPs)<sup>8,9</sup> or hybrid perovskite thin films as sensitizers of the TMO<sup>10–15</sup> are also being intensely studied. In all these schemes, crucial for the optimization of the photovoltaic efficiency is a thorough understanding of the mechanisms and time scales for charge injection from the sensitizer into the conduction band (CB) of the TMO substrate, and of the way charge carriers evolve in the latter. This has called for the development of experimental methods capable of selectively probing the dynamics of interfacial ET with high temporal resolution.

Time-resolved photoluminescence (PL) spectroscopy allows one to measure the radiative recombination processes in the sensitizer and to associate their quenching with the injection rate;<sup>16–20</sup> however, this approach can be ambiguous, as other quenching mechanisms may affect the dye, especially at long time scales. Transient absorption spectroscopy from the visible to the terahertz (THz) range probes the absorption of the injected electrons,<sup>9,21–33</sup> which can remain free in the CB or undergo trapping at defects and impurities.<sup>30</sup> However, the interpretation of the spectra is complicated by the overlap between absorption bands of different states of the adsorbate (ground, singlet, triplet and corresponding oxidized forms).

More importantly, the featureless nature of the free-carrier absorption in the TMO substrate hinders the extension of this technique to the case of solid-state sensitizers, because the signal from the TMO is overwhelmed by the intrinsic free-carrier absorption of the photoexcited sensitizer.<sup>34</sup> Recently, time-resolved X-ray absorption spectroscopy has been implemented to probe the ET into the TMO.<sup>38–35</sup> While providing an unambiguous fingerprint of the ET, this technique is mostly sensitive to localized charges in the TMO, because it maps the change of oxidation state of the metal. Furthermore, it can only be implemented at large-scale facilities such as synchrotrons or free-electron lasers.

An unambiguous, universal and laboratory-based probe of charge injection is therefore needed. In this regard, a simple and novel methodology can be based on the detection of specific spectroscopic signatures of the TMO of interest, as opposed to the rather featureless and nonspecific intraband absorption of free carriers in the CB. Natural candidates for such signatures are the high-energy excitons and interband transitions of the substrate, which in TMOs typically lie in the deep-ultraviolet (UV) below 400 nm (above 3.10 eV). A similar approach was recently implemented in the visible range by Wachtveitl and co-workers,<sup>40</sup> who detected the excitonic transitions of CdSe quantum dots after selective photoexcitation of a surface-bound alizarin dye injecting an electron. Demonstrating this methodology in the deep-UV has two main advantages: (i) In TMOs, upon electron injection into the CB, specific excitons and interband transitions can undergo pronounced changes through

Received: June 17, 2017

Published: August 1, 2017

various mechanisms, e.g., phase-space filling (PSF), Coulomb screening (CS), etc. Thus, appearance of these features in a visible pump/deep-UV continuum probe experiment provides a distinct signature of ET from the sensitizer, allowing one to monitor the evolution of the electrons in the CB; (ii) The deep-UV region is weakly affected by the free-carrier absorption signal, which scales as  $\lambda^p$  within the extended Drude model (where  $p > 1$  accounts for the scattering mechanisms that dominate in the material).<sup>39</sup> Although femtosecond deep-UV monochromatic pulses have been generated at wavelengths as short as 227 nm,<sup>41</sup> crucial for these experiments is the availability of broadband continuum pulses that can span the entire contour of the excitonic bands of TMOs. These pulses were recently demonstrated in the framework of ultrafast transient absorption and two-dimensional deep-UV spectroscopy.<sup>42,43</sup>

Using this technique, here we show that the electron injection from an external dye into the CB of two typical TMOs for DSSC applications results in a pronounced modification of their excitonic transitions. We use the *cis*-di(thiocyanato)bis(2,2'-bipyridyl-4,4'-dicarboxylate)ruthenium-(II) dye, known as N719, and both anatase TiO<sub>2</sub> and wurtzite ZnO NPs substrates. We observe that the broadening of the first exciton band dominates in the case of anatase TiO<sub>2</sub>, consistent with the presence of long-range CS by the injected electron density, whereas PSF dominates in wurtzite ZnO. These results offer a new methodology that can be applied to different samples (other TMOs and/or different sensitizers) to unambiguously probe interfacial ET.

## RESULTS AND DISCUSSION

The experimental methods are described in S1 and S2. Figure 1 shows the steady-state absorption spectra of the different

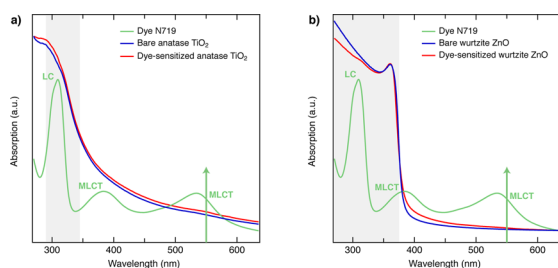


**Figure 1.** Steady-state absorption spectra of (a) N719 dye (green curve) in DMF, the colloidal solution of bare anatase TiO<sub>2</sub> NPs (blue curve) in acidic water and the colloidal solution of dye-sensitized anatase TiO<sub>2</sub> NPs (red curve) in DMF; (b) N719 dye (green curve) in DMF, the colloidal solution of bare wurtzite ZnO NPs (blue curve) in ethanol and the colloidal solution of dye-sensitized wurtzite ZnO NPs (red curve) in ethanol. The pump wavelength of 550 nm (2.25 eV) used for the pump–probe experiment is indicated by the green arrows and the probed broadband UV region is highlighted as a gray shaded area. The assignments of the MLCT bands and the LC band are also specified.

samples investigated here (discussed in S3). We first present the results obtained for the constituents of the sensitized system before describing those of the latter.

Excitation of the singlet metal-to-ligand charge-transfer (<sup>1</sup>MLCT, green arrows in Figure 1) state of N719 molecules in a dimethylformamide (DMF) solution leads to population of the <sup>3</sup>MLCT state, which has a lifetime of 20 ns.<sup>44</sup> The deep-UV (shaded area in Figure 1a) transient response of the dye system

upon excitation of its <sup>1</sup>MLCT state at 550 nm (2.25 eV) is shown in Figure 2a displaying the resulting color-coded

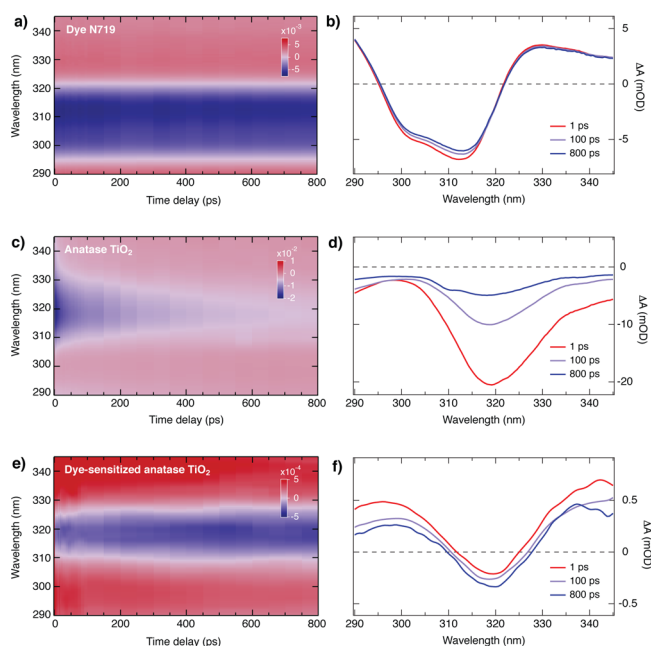


**Figure 2.** (a,c,e) Color-coded maps of  $\Delta A$  as a function of probe wavelength and time delay between pump and probe. (b,d,f)  $\Delta A$  spectra at selected delays of 1 ps (red curves), 100 ps (violet curves) and 800 ps (blue curves). (a,b) Visible pump/UV-probe  $\Delta A$  on the dye N719 in solution excited at 550 nm, with a fluence of 40  $\mu\text{J}/\text{cm}^2$ . (c,d) UV pump/UV probe  $\Delta A$  on a colloidal solution of bare anatase TiO<sub>2</sub> NPs, excited at 306 nm with a fluence of 176  $\mu\text{J}/\text{cm}^2$ . (e,f) Visible pump/UV probe experiment on a colloidal solution of N719 dye-sensitized anatase TiO<sub>2</sub> NPs, excited at 550 nm with a fluence of 168  $\mu\text{J}/\text{cm}^2$ .

differential absorption ( $\Delta A$ ) map as a function of probe wavelength and time delay between the visible pump and deep-UV probe (at a fluence of 40  $\mu\text{J}/\text{cm}^2$ ). Figure 2b shows the transients at specific time delays. A prominent negative feature appears between 295 and 325 nm, which corresponds to the bleach of the ligand-centered (LC, Figure 1) band due to depopulation of the ground state by the pump pulse. The regions to the blue and the red side of this bleach band are positive. All features (positive or negative) exhibit a long temporal behavior (Figure S2), characteristic of the promptly populated ( $\leq 30\text{--}40$  fs<sup>45,46</sup>) <sup>3</sup>MLCT state.<sup>44</sup> This implies that the positive features in Figure 2b are due to an excited state absorption of the <sup>3</sup>MLCT state. The weak evolution at early times of all features in Figure 2a is due to vibrational cooling processes.<sup>47</sup>

We now turn to the case of bare anatase TiO<sub>2</sub> NPs in an acidic aqueous solution. As the indirect optical band gap of the material lies at 387 nm (3.20 eV), we pump the sample at 306 nm (4.05 eV) to excite uncorrelated electron–hole pairs via direct interband transitions. Figure 2c shows  $\Delta A$  as a function of probe wavelength and time delay between the UV pump and probe pulses (at a fluence of 176  $\mu\text{J}/\text{cm}^2$ ). Figure 2d shows transients at specific time delays. A strong ( $\Delta A \sim 10^{-2}$ ) negative signal appears over the entire probe range, with a pronounced feature centered around 320 nm (3.87 eV), which undergoes a clear recovery over the measured 800 ps range (Figure 2d). This feature corresponds to the direct exciton of

anatase  $\text{TiO}_2$ ,<sup>48</sup> which has a large binding energy of  $\sim 180$  meV as recently demonstrated in ref 49. It is hidden in the steady-state absorption spectrum of colloidal  $\text{TiO}_2$  NPs (blue curve, Figure 1a) due to the strong scattering of the UV light.<sup>49,50</sup> These scattering effects are canceled in a pump–probe scheme, thus allowing one to reveal the contours of the excitonic feature.<sup>49</sup> The negative signal is due to the bleach of the excitonic resonance because the CB final states involved in the formation of the exciton are filled upon direct band gap excitation (vide infra). The strength of the bleach depends on the density of the photogenerated carriers, therefore its decay reflects the recombination kinetics. We also performed a pump fluence dependence study of the bleach signal by tuning the photoexcited carrier density between  $8.0 \times 10^{19}$  and  $8.4 \times 10^{20} \text{ cm}^{-3}$  (see Figure 4a,b in ref 51). The maximum signal amplitude is found to scale linearly in the investigated fluence regime and the width of the exciton line shape slightly increases as a function of photoexcited carrier density. Moreover, to rule out multiphoton absorption processes in the measurements on the dye-sensitized anatase  $\text{TiO}_2$  (shown below), we also investigated the bare anatase  $\text{TiO}_2$  NPs upon below-gap photoexcitation at 400 nm (3.10 eV) and 550 nm (2.25 eV). No signal is detected even at fluences as high as  $34 \text{ mJ/cm}^2$ . This observation also implies that defect-assisted transitions contributing to the tail of the steady-state absorption spectrum are not sufficient to induce a detectable bleach of the excitonic transition.

Now, we analyze the case of N719-sensitized anatase  $\text{TiO}_2$  NPs dispersed in DMF. We excite the  $^1\text{MLCT}$  state of the dye at 550 nm (2.25 eV) and probe in the deep-UV range. Figure 2e shows  $\Delta A$  as a function of probe wavelength and time delay between the visible pump and the UV probe, and Figure 2f shows transient spectra at specific time delays. The latter exhibit the same shape as in the case of bare  $\text{TiO}_2$  NPs (Figure 2d), except that the signal now spans a region of negative (between 312 and 325 nm) and two regions of positive absorption (on both sides of the negative signal). Moreover, the overall signal is about 2 orders of magnitude smaller ( $\Delta A \sim 10^{-4}$ ) than the one obtained in the case of bare anatase  $\text{TiO}_2$  NPs. We also performed a fluence dependence between 80 and  $340 \mu\text{J/cm}^2$  (Figure S3). The transients at different pump fluences are compared in Figure S4 and they reflect the same behavior: The positive and negative signal amplitudes scale linearly with fluence. The normalized transients at fixed time delay (Figure S4b) show a slight broadening of the feature at 320 nm with pump fluence.

By comparing the transient spectra at 1 ps (rescaled for clarity) obtained from the three separate experiments in Figure 3a, we confirm the almost analogous spectral response of bare and sensitized anatase NPs, except for a vertical shift and the above-mentioned orders of magnitude difference in signal amplitude. In contrast, no common features are shared with the response of the N719 dye under identical excitation conditions. This clearly points to charge injection from the dye into the anatase  $\text{TiO}_2$  NPs that leads to changes of the excitonic feature. The occurrence of charge injection is further confirmed by Figure 3b, which shows the kinetics of the signals at 320 nm for both bare and dye-sensitized NPs. The negative signal of the bare NPs has a resolution-limited rise ( $\tau_{\text{NP1}} \sim 150$  fs), which is due to the electron–hole cooling to the band edges.<sup>51</sup> Then, the signal amplitude decays on the ps to hundreds of ps time scale, due to recombination of uncorrelated electron–hole pairs across the band gap of the material. Fits with four exponential

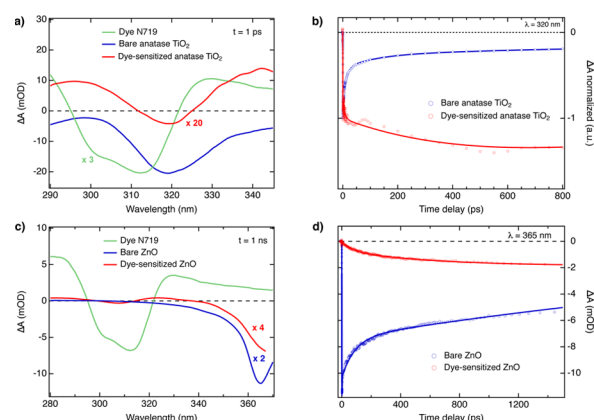


**Figure 3.** (a) Comparison of the  $\Delta A$  spectra measured in the three separate experiments of Figure 2 at a time delay of 1 ps. The transient spectrum of the dye N719 is shown in green, the one of the bare anatase  $\text{TiO}_2$  NPs in blue, and the one of the dye-sensitized anatase  $\text{TiO}_2$  NPs in red. (b) Comparison of the normalized  $\Delta A$  temporal traces at a probe wavelength of 320 nm. The temporal evolution of the bare anatase  $\text{TiO}_2$  is shown in blue, the one of the dye-sensitized anatase  $\text{TiO}_2$  NPs in red. Dots represent experimental data points, solid lines are fittings (see text). (c) Comparison of the  $\Delta A$  spectra measured in the wurtzite  $\text{ZnO}$  related experiments. The transient spectrum of the dye N719 is in green (1 ps after excitation, fluence  $40 \mu\text{J/cm}^2$ ). The transient spectra of bare (blue, fluence  $63 \mu\text{J/cm}^2$ ) and dye-sensitized (red, fluence  $740 \mu\text{J/cm}^2$ ) wurtzite  $\text{ZnO}$  are given 1 ns after excitation. (d) Comparison of the time traces measured at 365 nm in the case of bare  $\text{ZnO}$  NPs under 295 nm excitation (blue curve) and N719 dye-sensitized  $\text{ZnO}$  NPs under 550 nm excitation (red curve). Dots represent experimental data; lines are fits.

functions provide time constants of  $\tau_{\text{NP2}} = 1.6 \pm 0.12$  ps,  $\tau_{\text{NP3}} = 10 \pm 1.4$  ps,  $\tau_{\text{NP4}} = 50 \pm 1.7$  ps and  $\tau_{\text{NP5}} = 423 \pm 15$  ps, as reported in ref 51. Because anatase  $\text{TiO}_2$  is an indirect band gap insulator, the recombination proceeds slowly and can be accelerated only through the assistance of defect and impurity states.<sup>49</sup> In the case of dye-sensitized NPs, the signal (Figures 3b and S5) in the central (negative) part of the spectrum also appears promptly, which indicates the presence of a dominating sub-ps component in the charge injection from the external dye. Thereafter, the response undergoes a further growth. The kinetic traces of the positive and negative regions of the transient spectra are shown in Figure S5. The positive parts exhibit a prompt rise followed by a multi-exponential decay. The responses of the positive and negative parts can be globally fit using the same set of time constants: a resolution-limited rise,  $\tau_{\text{D1}} \sim 150$  fs, and decay/rise (positive/negative parts, respectively) components,  $\tau_{\text{D2}} = 22$  ps and  $\tau_{\text{D3}} = 1.1$  ns. This suggests a common origin for the growth and decays of the various parts of the signal, which we rationalize below.

Previous visible<sup>23,29,33,53</sup> and THz<sup>24</sup> transient absorption studies on N719- or N3-sensitized  $\text{TiO}_2$  reported a multimodal electron injection: A prompt one at very short times ( $\ll 100$  fs) from the initially accessed Franck–Condon  $^1\text{MLCT}$  state, followed by slower injection from the rapidly populated<sup>20</sup> long-lived  $^3\text{MLCT}$  state, with typical time scales of 1, 10, 60 and  $>200$  ps. The time scales we extract from Figures 3b and S5 reflect this multimodal injection regime. For the purpose of our discussion, we remark that these long time scans suffered from drifts that caused the modulations around 50 and 550 ps. As such, the extracted time scales offer only a qualitative indication of the kinetics, but this does not affect our conclusions.



To rationalize the difference in transient spectra obtained upon above-gap excitation and charge injection, we first rule out the involvement of the dye on the spectral response of Figure 2e,f. The lack of an LC bleach can be explained by the fact that the dye coverage of the NPs is such that their concentration is very low (see S1) and their signal is very weak. Furthermore, the LC band around 310 nm is not sensitive to a change of the Ru oxidation state.<sup>54</sup>

We now link the results obtained on bare and sensitized anatase TiO<sub>2</sub> to the details of the band structure of this TMO (Figure 4). In anatase TiO<sub>2</sub>, the top of the VB is close to the X

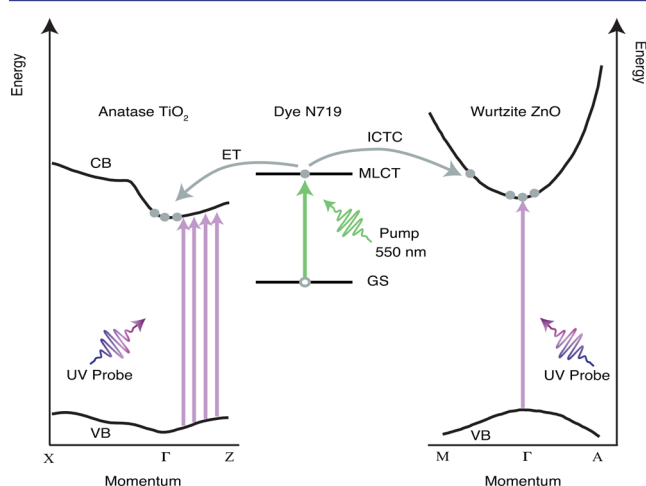


**Figure 4.** Schematic representation of the deep-UV based detection of the ultrafast ET dynamics in sensitized TiO<sub>2</sub> (left) and ZnO (right) NPs. The pump photon at 550 nm (green arrow) excites the MLCT state of the N719 dye, which then injects an electron directly into the CB of anatase TiO<sub>2</sub> or forms an interfacial charge-transfer complex (ICTC) at the wurtzite ZnO surface. The broadband deep-UV pulse (violet arrows) probes the exciton features at 320 and 365 nm for TiO<sub>2</sub> and ZnO, respectively. The direct transitions contributing to this collective state lie in the middle of the  $\Gamma$ -Z region of the Brillouin zone of anatase TiO<sub>2</sub>. The sharp exciton line in wurtzite ZnO comes from the  $\Gamma$  point of the Brillouin zone. The band structure of anatase TiO<sub>2</sub> has been adapted from ref 48, the one from wurtzite ZnO from ref 52.

point of the Brillouin zone (BZ), whereas the bottom of the CB lies at the  $\Gamma$  point.<sup>49</sup> The exciton state is a collective excitation arising from a manifold of direct interband transitions in the middle of the  $\Gamma$ -Z direction, in which the CB and VB dispersions are almost parallel. In contrast, based on symmetry arguments, the states around the  $\Gamma$  point are not expected to participate to the exciton transition.<sup>48,49</sup> In the case of above-gap excitation of bare anatase TiO<sub>2</sub>, the transient spectral response can be understood as the combination of two optical nonlinearities: PSF and long-range CS.<sup>55</sup> PSF causes a reduction of the exciton oscillator strength by reducing the number of single-particle states contributing to the transition. It is akin to bleaching in molecules but, in solids, the occupancy of both the VB and the CB may contribute to the signal, especially in the case of an indirect band gap material like anatase TiO<sub>2</sub>. Long-range CS causes a broadening of the exciton line width, as supported by our steady-state absorption spectra as a function of  $n$ -doping<sup>49</sup> and by the dependence of the exciton line width with pump fluence mentioned above.<sup>51</sup> In the bare NPs, the density of electrons in the CB is high enough ( $>5 \times 10^{19} \text{ cm}^{-3}$ , see S4) to fill the single-particle states involved in the excitonic transition, and the signal is dominated by the contribution of

PSF. This overwhelms any positive signal associated with free-carrier absorption and it results in a negative signal over the entire spectral range (Figure 2c,d). On the other hand, broadening of the excitonic band is caused by CS, which we observe in the pump fluence dependence.<sup>51</sup> This is further supported by the similar shape of the transient signal in sensitized NPs (Figure 3a). Thus, for bare NPs, the transient signal is dominated by PSF and CS. In contrast, in the case of dye-sensitized NPs, PSF becomes extremely weak, as the electron density is 2 orders of magnitude smaller ( $<10^{18} \text{ cm}^{-3}$ , see S4), and it is expected to be located mostly at the bottom of the CB at the  $\Gamma$  point in contrast to the above-gap excitation where a large number of states along the  $\Gamma$ -Z reciprocal direction are involved (Figure 4). Under these conditions, long-range CS is the only significant effect on the excitonic transition and, because it results in a broadening of the excitonic band, the transient adopts a second derivative-like shape with a negative central part and two positive contributions in the wings. However, in Figure 2f, the area under the positive parts of the signal is larger than in the negative one, implying the presence of an additional positive contribution, which is due to residual weak free-carrier absorption in the deep-UV (the free-carrier absorption scales as  $\lambda^p$  as indicated above). The dominant contribution due to long-range CS also explains the kinetics of the positive and negative parts of the signal shown in Figure S5. Indeed, the initial ( $<100 \text{ fs}$ ) injection promptly generates the negative and positive parts due to broadening of the exciton line shape. Further injection on multiexponential time scales will accentuate the broadening, generating a more pronounced negative part but decreasing the amplitude of the positive wings. Thus, whereas the negative part continues growing in amplitude, the positive wings first promptly increase, then decrease as seen in Figure S5. However, the time constants in all three parts of the signal should be identical, as is actually the case. Another signature of the enhanced broadening is provided by the temporal evolution of the zero-crossing energies in Figure 2f. A pictorial representation of the deep-UV based detection of the ultrafast ET dynamics in sensitized TiO<sub>2</sub> NPs is provided in Figure 4.

To extend the present approach to other systems, we also investigated the case of wurtzite ZnO NPs. Its main difference with anatase TiO<sub>2</sub> resides in its direct band gap (Figure 4), with the minimum energy required for the optical excitation of 360 nm (3.44 eV) at the  $\Gamma$  point.<sup>56,57</sup> The steady-state spectra of the bare and dye-sensitized ZnO NPs are given in Figure 1b. The resonance at  $\sim 365 \text{ nm}$  is due to a direct exciton with a binding energy of  $\sim 60 \text{ meV}$ .<sup>58</sup> Upon N719 dye adsorption, the absorbance increases below the optical band gap mainly because of the modification of the scattering cross section of the NPs in the low dye coverage limit. The MLCT transition at 540 nm becomes visible with increasing concentration (Figure S1b).

Figure 3c shows the transient spectrum of bare wurtzite ZnO NPs pumped at 295 nm (4.20 eV), well above the optical gap of the material to excite uncorrelated electron-hole pairs (fluence  $63 \mu\text{J}/\text{cm}^2$ ). The transient signal exhibits a negative Lorentzian line shape centered at the exciton position around 365 nm. The kinetic trace of the transient spectrum (blue curve, Figure 3d) shows a prompt appearance of the bleach followed by a multiexponential recovery exceeding several ns, in agreement with PL studies.<sup>59,60</sup> The fit provides time constants of  $\tau_{NP1} = 1.1 \pm 0.1 \text{ ps}$ ,  $\tau_{NP2} = 87.6 \pm 1.0 \text{ ps}$  and  $\tau_{NP3} = 3.9 \pm 0.4 \text{ ns}$  for the decay. The initial ps time constant was reported by time-

resolved THz,<sup>61</sup> PL<sup>62</sup> and transient reflectivity,<sup>63</sup> commonly assigned to the initial relaxation of the electron–hole plasma. The longer time constants widely differ depending on excitation conditions and sample preparation as shown by time-resolved PL.<sup>60,62,64</sup>

The transient signal of the dye-sensitized wurtzite ZnO NPs upon 550 nm excitation (fluence 740  $\mu\text{J}/\text{cm}^2$ ) is also shown in Figure 3(a). It exhibits a negative (bleach) region centered at 310 nm with positive wings, which reflect the transient absorption spectrum of the N719 molecules. These features have the same kinetics as the molecule in the solvent (Figure S6) and are therefore due to species not bound to ZnO NPs. In addition, a negative signal appears at  $\sim 365$  nm, which coincides with the first exciton seen in bare ZnO NPs. It increases in amplitude over time as shown by the temporal trace (red curve) in Figure 3b. The slow rise of the bleach signal occurs on a time scale of several tens to hundreds of ps (fits provide  $\tau_{D1} = 64$  ps and  $\tau_{D2} = 590$  ps), as already reported using THz,<sup>65</sup> mid-infrared,<sup>66</sup> near-infrared<sup>24,67–69</sup> probes of injection from different dye sensitizers. The formation of an interfacial charge-transfer complex at the ZnO surface has been invoked to explain this signal growth.<sup>24,66,68,70–72</sup> We will revisit it in detail in a separate paper. Because the transient signal of the dye has a positive contribution in the spectral range of the exciton in ZnO (Figure 3a), the signal above 340 nm is unambiguously due to the bleach of the excitonic transition in ZnO. The maximum amplitude of this signal at 1 ns after excitation is approximately 1 order of magnitude lower than in the bare ZnO, in line with our estimate of the number of injected charge carriers relative to the bare NP case (see S4). Note that in sensitized ZnO, different from anatase TiO<sub>2</sub>, the bleach band does not exhibit a second derivative-like shape, which rules out CS. Instead, the main signal is negative and sharp, pointing to a dominant PSF contribution that is a consequence of the electron relaxation near the  $\Gamma$  point and subsequent exciton bleaching. This important result underlines the fundamental difference of the optical nonlinearities between indirect (e.g., anatase TiO<sub>2</sub>) and direct (e.g., wurtzite ZnO) band gap insulators. The dynamics of the electron injection into the CB of ZnO NPs can be monitored from this negative signal and show the generality of our methodology to exploit high-energy excitations in TMO substrates as a spectroscopic fingerprint of electron injection. A schematic representation of the electron injection in dye-sensitized ZnO is given in Figure 4.<sup>52</sup>

## CONCLUSIONS

In summary, our results demonstrate the use of the deep-UV excitonic bands for probing interfacial ET in dye-sensitized TMOs, showing that electron injection strongly affects the exciton bands of the materials: TiO<sub>2</sub> anatase undergoes long-range Coulomb screening, as most single-particle states contributing to the exciton are situated in the middle of the  $\Gamma$ -Z points of the BZ, i.e. far from the bottom of the CB. On the other hand, wurtzite ZnO undergoes phase-space filling due to thermalization of the injected electrons populating the states involved in the formation of the exciton at the  $\Gamma$  point. The kinetic traces of the electron injection in both materials map out the behavior reported by other methods, thus establishing an elegant substrate-specific methodology for probing interfacial ET in sensitized TMOs by exploiting the excitonic transitions. Our results pave the way to the use of this approach

in the case of solid-state sensitizers, as the absorption of the CB electrons in the sensitizer is strongly reduced in the deep-UV.

## ASSOCIATED CONTENT

### Supporting Information

The Supporting Information is available free of charge on the ACS Publications website at DOI: 10.1021/jacs.7b06322.

Materials and methods, and additional results (PDF)

## AUTHOR INFORMATION

### Corresponding Author

\*maged.chergui@epfl.ch

### ORCID

Maged Chergui: 0000-0002-4856-226X

### Notes

The authors declare no competing financial interest.

## ACKNOWLEDGMENTS

We thank Giulia Grancini for useful discussions. We acknowledge financial support from the Swiss NSF via the NCCR:MUST and the contracts No. 206021-157773 and 407040-154056 (PNR 70), and the European Research Council Advanced Grant H2020 ERCEA 695197 DYNAMOX.

## REFERENCES

- (1) Nazeeruddin, M. K.; Baranoff, E.; Grätzel, M. *Sol. Energy* **2011**, 85, 1172–1178.
- (2) Kalyanasundaram, K.; Zakeeruddin, S. M.; Grätzel, M. *Chimia* **2011**, 65, 738–742.
- (3) Hagfeldt, A.; Grätzel, M. *Acc. Chem. Res.* **2000**, 33, 269–277.
- (4) Zhang, Q.; Chou, T. P.; Russo, B.; Jenekhe, S. A.; Cao, G. *Angew. Chem., Int. Ed.* **2008**, 47, 2402–2406.
- (5) Nakata, K.; Fujishima, A. *J. Photochem. Photobiol., C* **2012**, 13, 169–189.
- (6) Linsebigler, A. L.; Lu, G.; Yates, J. T., Jr. *Chem. Rev.* **1995**, 95, 735–758.
- (7) Lee, K. M.; Lai, C. W.; Ngai, K. S.; Juan, J. C. *Water Res.* **2016**, 88, 428–448.
- (8) Furube, A.; Du, L.; Hara, K.; Katoh, R.; Tachiya, M. *J. Am. Chem. Soc.* **2007**, 129, 14852–14853.
- (9) Du, L.; Furube, A.; Hara, K.; Katoh, R.; Tachiya, M. *J. Phys. Chem. C* **2010**, 114, 8135–8143.
- (10) Stranks, S. D.; Eperon, G. E.; Grancini, G.; Menelaou, C.; Alcocer, M. J. P.; Leijtens, T.; Herz, L. M.; Petrozza, A.; Snaith, H. J. *Science* **2013**, 342, 341–344.
- (11) Marchioro, A.; Teuscher, J.; Friedrich, D.; Kunst, M.; van de krol, R.; Moehl, T.; Grätzel, M.; Moser, J.-E. *Nat. Photonics* **2014**, 8, 250–255.
- (12) Liu, M.; Johnston, M. B.; Snaith, H. J. *Nature* **2013**, 501, 395–398.
- (13) Hodes, G. *Science* **2013**, 342, 317–318.
- (14) Lee, M. M.; Teuscher, J.; Miyasaka, T.; Murakami, T. N.; Snaith, H. J. *Science* **2012**, 338, 643–647.
- (15) Kojima, A.; Teshima, K.; Shirai, Y.; Miyasaka, T. *J. Am. Chem. Soc.* **2009**, 131, 6050–6051.
- (16) Willig, F.; Eichberger, R.; Sundaresan, N. S.; Parkinson, B. A. *J. Am. Chem. Soc.* **1990**, 112, 2702–2707.
- (17) Rosenwaks, Y.; Thacker, B. R.; Ahrenkiel, R. K.; Nozik, A. J. *J. Phys. Chem.* **1992**, 96, 10096–10098.
- (18) Rehm, J. M.; McLendon, G. L.; Nagasawa, Y.; Yoshihara, K.; Moser, J.; Grätzel, M. *J. Phys. Chem.* **1996**, 100, 9577–9578.
- (19) Heimer, T. A.; Meyer, G. J. *J. Lumin.* **1996**, 70, 468–478.
- (20) Bräm, O.; Cannizzo, A.; Chergui, M. *Phys. Chem. Chem. Phys.* **2012**, 14, 7934–4.

- (21) Teuscher, J.; Décoppet, J.-D.; Punzi, A.; Zakeeruddin, S. M.; Moser, J.-E.; Grätzel, M. *J. Phys. Chem. Lett.* **2012**, *3*, 3786–3790.
- (22) Pijpers, J. J. H.; Ulbricht, R.; Derossi, S.; Reek, J. N. H.; Bonn, M. *J. Phys. Chem. C* **2011**, *115*, 2578–2584.
- (23) Pellnor, M.; Myllyperkiö, P.; Korppi-Tommola, J.; Yartsev, A.; Sundström, V. *Chem. Phys. Lett.* **2008**, *462*, 205–208.
- (24) Němec, H.; Rochford, J.; Taratula, O.; Galoppini, E.; Kužel, P.; Polívka, T.; Yartsev, A.; Sundström, V. *Phys. Rev. Lett.* **2010**, *104*, 197401–4.
- (25) Němec, H.; Kužel, P.; Sundström, V. *Phys. Rev. B: Condens. Matter Mater. Phys.* **2009**, *79*, 115309–7.
- (26) Negre, C. F. A.; Milot, R. L.; Martini, L. A.; Ding, W.; Crabtree, R. H.; Schmuttenmaer, C. A.; Batista, V. S. *J. Phys. Chem. C* **2013**, *117*, 24462–24470.
- (27) Katoh, R.; Furube, A.; Barzykin, A. V.; Arakawa, H.; Tachiya, M. *Coord. Chem. Rev.* **2004**, *248*, 1195–1213.
- (28) Kallioinen, J.; Benkö, G.; Myllyperkiö, P.; Khriachtchev, L.; Skärman, B.; Wallenberg, R.; Tuomikoski, M.; Korppi-Tommola, J.; Sundström, V.; Yartsev, A. P. *J. Phys. Chem. B* **2004**, *108*, 6365–6373.
- (29) Kallioinen, J.; Benkö, G.; Sundström, V.; Korppi-Tommola, J. E. I.; Yartsev, A. P. *J. Phys. Chem. B* **2002**, *106*, 4396–4404.
- (30) Huber, R.; Spörlein, S.; Moser, J.-E.; Grätzel, M.; Wachtveitl, J. *J. Phys. Chem. B* **2000**, *104*, 8995–9003.
- (31) Tamaki, Y.; Hara, K.; Katoh, R.; Tachiya, M.; Furube, A. *J. Phys. Chem. C* **2009**, *113*, 11741–11746.
- (32) Benkö, G.; Myllyperkiö, P.; Pan, J.; Yartsev, A. P.; Sundström, V. *J. Am. Chem. Soc.* **2003**, *125*, 1118–1119.
- (33) Anderson, N. A.; Lian, T. *Coord. Chem. Rev.* **2004**, *248*, 1231–1246.
- (34) Ponseca, C. S., Jr.; Savenije, T. J.; Abdellah, M.; Zheng, K.; Yartsev, A.; Pascher, T.; Harlang, T.; Chabera, P.; Pullerits, T.; Stepanov, A.; Wolf, J.-P.; Sundström, V. *J. Am. Chem. Soc.* **2014**, *136*, 5189–5192.
- (35) Katz, J. E.; Gilbert, B.; Zhang, X.; Attenkofer, K.; Falcone, R. W.; Waychunas, G. A. *J. Phys. Chem. Lett.* **2010**, *1*, 1372–1376.
- (36) Katz, J. E.; Zhang, X.; Attenkofer, K.; Chapman, K. W.; Frandsen, C.; Zarzycki, P.; Rosso, K. M.; Falcone, R. W.; Waychunas, G. A.; Gilbert, B. *Science* **2012**, *337*, 1200–1203.
- (37) Rittmann-Frank, M. H.; Milne, C. J.; Rittmann, J.; Reinhard, M.; Penfold, T. J.; Chergui, M. *Angew. Chem., Int. Ed.* **2014**, *53*, 5858–5862.
- (38) Santomauro, F. G.; Lübcke, A.; Rittmann, J.; Baldini, E.; Ferrer, A.; Silatani, M.; Zimmermann, P.; Grübel, S.; Johnson, J. A.; Mariager, S. O.; Beaud, P.; Grolimund, D.; Borca, C.; Ingold, G.; Johnson, S. L.; Chergui, M. *Sci. Rep.* **2015**, *5*, 14834.
- (39) Yu, P. Y.; Cardona, M. *Fundamentals of semiconductors: physics and materials properties*, 3rd ed.; Springer: Dordrecht, 2005; Vol. 21.
- (40) Dworak, L.; Roth, S.; Wachtveitl, J. *J. Phys. Chem. C* **2017**, *121*, 2613–2619.
- (41) Larsen, J.; Madsen, D.; Poulsen, J.-A.; Poulsen, T. D.; Keiding, S. R.; Thøgersen, J. *J. Chem. Phys.* **2002**, *116*, 7997.
- (42) Consani, C.; Auböck, G.; van Mourik, F.; Chergui, M. *Science* **2013**, *339*, 1586–1589.
- (43) Auböck, G.; Consani, C.; van Mourik, F.; Chergui, M. *Opt. Lett.* **2012**, *37*, 2337.
- (44) Namekawa, A.; Katoh, R. *Chem. Phys. Lett.* **2016**, *659*, 154–158.
- (45) Bräm, O.; Messina, F.; El-Zohry, A. M.; Cannizzo, A.; Chergui, M. *Chem. Phys.* **2012**, *393*, 51–57.
- (46) Auböck, G.; Chergui, M. *Nat. Chem.* **2015**, *7*, 1–5.
- (47) Tarnovsky, A. N.; Gawelda, W.; Johnson, M.; Bressler, C.; Chergui, M. *J. Phys. Chem. B* **2006**, *110*, 26497–26505.
- (48) Chiodo, L.; García-Lastra, J. M.; Iacomino, A.; Ossicini, S.; Zhao, J.; Petek, H.; Rubio, A. *Phys. Rev. B: Condens. Matter Mater. Phys.* **2010**, *82*, 045207.
- (49) Baldini, E.; Chiodo, L.; Dominguez, A.; Palummo, M.; Moser, S.; Yazdi-Rizi, M.; Auböck, G.; Mallett, B. P. P.; Berger, H.; Magrez, A.; Bernhard, C.; Grioni, M.; Rubio, A.; Chergui, M. *Nat. Commun.* **2017**, *8*, 37.
- (50) Serpone, N.; Lawless, D.; Khairutdinov, R. *J. Phys. Chem.* **1995**, *99*, 16646–16654.
- (51) Baldini, E.; Palmieri, T.; Pomarico, E.; Auböck, G.; Chergui, M. *arXiv:1703.07818* **2017**.
- (52) Usuda, M.; Hamada, N.; Kotani, T.; van Schilfgaarde, M. *Phys. Rev. B: Condens. Matter Mater. Phys.* **2002**, *66*, 125101.
- (53) Myllyperkiö, P.; Benkö, G.; Korppi-Tommola, J.; Yartsev, A. P.; Sundström, V. *Phys. Chem. Chem. Phys.* **2008**, *10*, 996–1002.
- (54) Kalyanasundaram, K. *Coord. Chem. Rev.* **1982**, *46*, 159–244.
- (55) Hunsche, S.; Leo, K.; Kurz, H.; Kohler, K. *Phys. Rev. B: Condens. Matter Mater. Phys.* **1994**, *49*, 16565–16568.
- (56) Labat, F.; Ciofini, I.; Adamo, C. *J. Chem. Phys.* **2009**, *131*, 044708–12.
- (57) Ozawa, K.; Sawada, K.; Shirotori, Y.; Edamoto, K. *J. Phys.: Condens. Matter* **2005**, *17*, 1271–1278.
- (58) Mang, A.; Reimann, K.; Rubenacke, S. *Solid State Commun.* **1995**, *94*, 251–254.
- (59) Han, N. S.; Shim, H. S.; Seo, J. H.; Kim, S. Y.; Park, S. M.; Song, J. K. *J. Appl. Phys.* **2010**, *107*, 084306.
- (60) Koida, T.; Chichibu, S. F.; Uedono, A.; Tsukazaki, A.; Kawasaki, M.; Sota, T.; Segawa, Y.; Koinuma, H. *Appl. Phys. Lett.* **2003**, *82*, 532–534.
- (61) Hendry, E.; Koeberg, M.; Bonn, M. *Phys. Rev. B: Condens. Matter Mater. Phys.* **2007**, *76*, 045214–6.
- (62) Bauer, C.; Boschloo, G.; Mukhtar, E.; Hagfeldt, A. *Chem. Phys. Lett.* **2004**, *387*, 176–181.
- (63) Versteegh, M. A. M.; Kuis, T.; Stoof, H. T. C.; Dijkhuis, J. I. *Phys. Rev. B: Condens. Matter Mater. Phys.* **2011**, *84*, 035207–19.
- (64) Guo, B.; Ye, Z.; Wong, K. S. *J. Cryst. Growth* **2003**, *253*, 252–257.
- (65) Tiwana, P.; Docampo, P.; Johnston, M. B.; Snaith, H. J.; Herz, L. M. *ACS Nano* **2011**, *5*, 5158–5166.
- (66) Stockwell, D.; Yang, Y.; Huang, J.; Anfuso, C.; Huang, Z.; Lian, T. *J. Phys. Chem. C* **2010**, *114*, 6560–6566.
- (67) Anderson, N. A.; Ai, X.; Lian, T. *J. Phys. Chem. B* **2003**, *107*, 14414–14421.
- (68) Furube, A.; Katoh, R.; Hara, K. *Surf. Sci. Rep.* **2014**, *69*, 389–441.
- (69) Asbury, J. B.; Hao, E.; Wang, Y.; Ghosh, H. N.; Lian, T. *J. Phys. Chem. B* **2001**, *105*, 4545–4557.
- (70) Siefertmann, K. R.; et al. *J. Phys. Chem. Lett.* **2014**, *5*, 2753–2759.
- (71) Furube, A.; Katoh, R.; Hara, K.; Murata, S.; Arakawa, H.; Tachiya, M. *J. Phys. Chem. B* **2003**, *107*, 4162–4166.
- (72) Borgwardt, M.; Wilke, M.; Kampen, T.; Mähl, S.; Xiao, M.; Spiccia, L.; Lange, K. M.; Kiyan, I. Y.; Aziz, E. F. *Sci. Rep.* **2016**, *6*, 1–7.